Efficiency and Lifetime Analysis of Several Airborne Wind Energy Electrical Drive Concepts

Bakr Bagaber, Daniel Heide, Bernd Ponick and Axel Mertens
LEIBNIZ UNIVERSITY HANNOVER
Institute for Drive Systems and Power Electronics
Hannover, Germany
Phone: +49 (0) 511-762-3766
Email: bakr.bagaber@ial.uni-hannover.de
URL: www.ial.uni-hannover.de

Acknowledgments

This work was supported by the German Ministry of Economics and Technology (BMWi) – 0324217D.

Keywords

≪Wind-generator systems≫, ≪Voltage Source Converter (VSC)≫, ≪Parallel operation≫, ≪Thermal cycling≫, ≪Lifetime≫, ≪Permanent Magnet Synchronous Generator≫

Abstract

Several electrical drive concepts and control strategies for airborne wind energy systems are compared in this work. The results suggest that the proposed modified kite trajectory control and the parallel drive concept can indeed reduce the required silicon chip area and prolong the converter's lifetime without significantly impacting the overall system efficiency. The compromise is however, a higher system complexity and larger torque ripples which could impact the noise profile of the electrical machine. The investigation also reveals that the power converter size is influenced by the installation location and the associated wind class. Where installations around land agricultural areas have the biggest impact on the drive train because of the high wind turbulence.

Introduction

Airborne wind energy systems (AWES) are a new class of wind generators promising to harness wind at high altitudes above 200 meters in a cost-effective way [2]. Several concepts of AWES are under research, among which the pumping cycle (PC) type has already reached a market commercialization stage [3]. The system consists of a flying soft kite connected to a ground-based electrical machine by means of a strong tether; a control pod attached to the kite is used for steering. The principle of operation can be understood with the help of Fig. 1a. The cycle is initialized by positioning the kite at a suitable altitude against the wind direction in phase one. In phase two, reel-out (generation) starts by maneuvering the kite in a crosswind direction at a certain wind window angle (ϑ). The crosswind principle exploits the lift-to-drag ratio (E) to induce high apparent wind speed -and lift force- which maximizes the extraction of power [4]. Once the tether is almost entirely winched out, the third phase starts (transition phase). The kite is steered towards the zenith position ($\vartheta = 90$). During this transfer phase, the machine decelerates rapidly towards zero, while the torque remains high. Eventually, the fourth phase (reel-in) begins. The electric machine accelerates as a motor to pull the kite into lower elevations. Reel-in is usually accomplished under maximum speed at very wide angles ($\vartheta > 90$) to reduce the tether force.

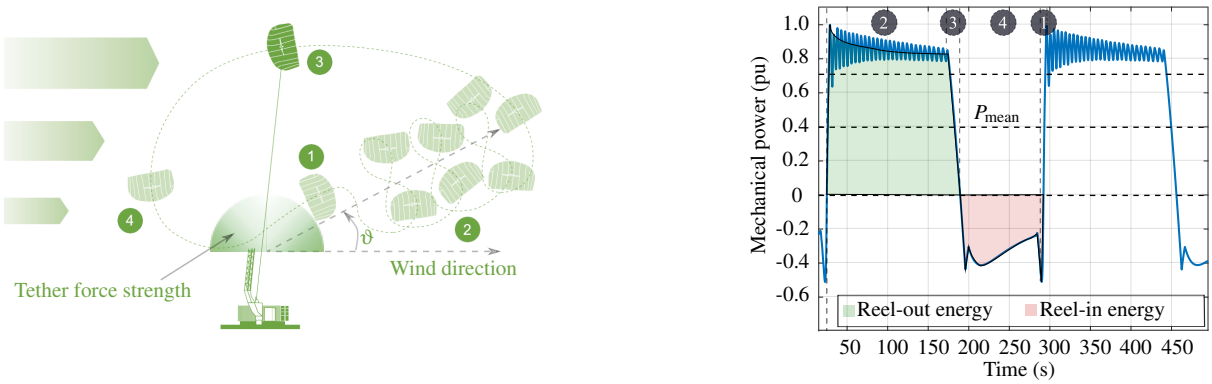

(a) Complete pumping cycle.

(b) Typical power profile.

Fig. 1: principle of operation of a typical PC-AWES: (1) Start/restart, (2) Reel-out (generation), (3) Transfer (generation), (4) Reel-in (consumption). Modified from [1].

The resulting variable power profile is shown in Fig. 1b. The impact of this unusual load-cycle on the dimensioning and lifetime of a standard machine drive comprising a three-phase voltage source converter (VSC) driving a permanent magnet synchronous machine (PMSM) was investigated in [5]. It was concluded that the thermal cycles because of the reel-out/reel-in duality, as well as the thermal cycles due to speed reversal (low frequency at maximum torque), produce large stress on the free-wheeling diodes baseplate to case solder joints. Therefore, the converter needs to be significantly over-scaled to reach the target lifetime of 20 years. This would increase the capital cost and the switching losses of the converter.

To mitigate this problem, an alternative drive concept based on the parallel connection of a VSC and a passive diode rectifier as depicted in Fig. 2 was proposed in [6]. This concept is capable of decoupling the influence of the reel-out/reel-in thermal cycles, which should allow for a cost-effective and efficient over dimensioning of the passive diode rectifier. It was also found that the size of the VSC can be further reduced through an adjusted kite control during the transfer phase to allow for speed reversal at lower torques. Reducing the switching frequency at lower operational speeds can further contribute to a reduction of the required VSC size [6].

The goal of this work is to first extend the comparison between the two drive concepts in terms of their lifetime and efficiency, including the DC-DC converter under ideal and turbulent wind conditions. Sec-

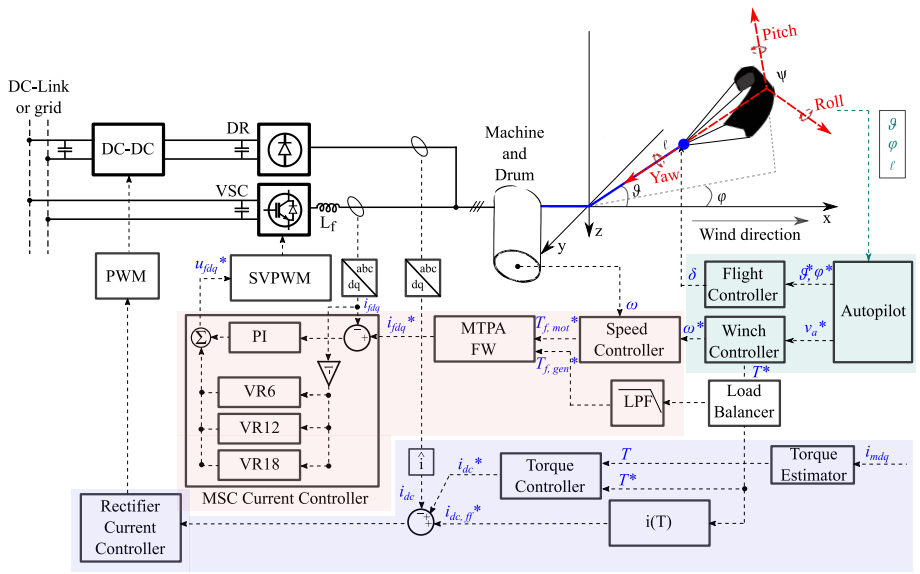

Fig. 2: Overview of the system model and control.

ond, to evaluate the impact of the parallel concept on the electrical machine. The investigation is based on the simulation model of Fig. 2, which is used for estimating the thermal performance of the power electronic converters. A 2D FEM model is used for designing the PMSM and analyzing its mechanical, electrical, and thermal performance. Finally, analytical models are used for sizing the converters to meet the lifetime goal of 20 years.

AWES Drive Concepts

In this work, two drive concepts are compared. The first is a standard machine drive consisting of a PMSM and a VSC. The VSC is controlled using maximum torque per ampere (MTPA) and field-weakening (FW). The second concept depicted in Fig. 2 was first introduced in [6]. It comprises a PMSM driven by a VSC paralleled with a diode rectifier (DR) and a DC-DC converter.

The control principle of the parallel drive concept can be explained as follows, during reel-out, the system operates under torque control mode, in which the kite controller adjusts the winching speed. The diode rectifier controls the machine torque using a unidirectional DC-DC converter, and the VSC acts as a current sink through which a small part of the machine current deviates according to the command of the load balancer. This control concept allows the cheaper, more robust diode rectifier to carry most of the reel-out power using a near unity power factor. Control of the VSC current is only possible through the use of the series decoupling inductor L_f, which allows the converter to operate as a controlled current source/sink. It also facilitates the selective damping of the odd non-triple harmonics (5th, 7th, 11th, 13th, ...) generated by the diode rectifier in the VSC branch using several vector-resonant (VR) controllers. A depiction of the system currents with and without the VR controllers is availabe in Fig. 3. During reel-in, the VSC operates in speed control mode using standard MTPA and FW techniques; the rectifier branch is turned off, and the kite controller adjusts the system torque [6].

System modeling

Pumping Cycle AWES Model

The dynamic model of the PC-AWES can be explained with the help of Fig. 2. The kite position can be described by means of three state variables in the polar coordinate system, the wind window angle ϑ, the

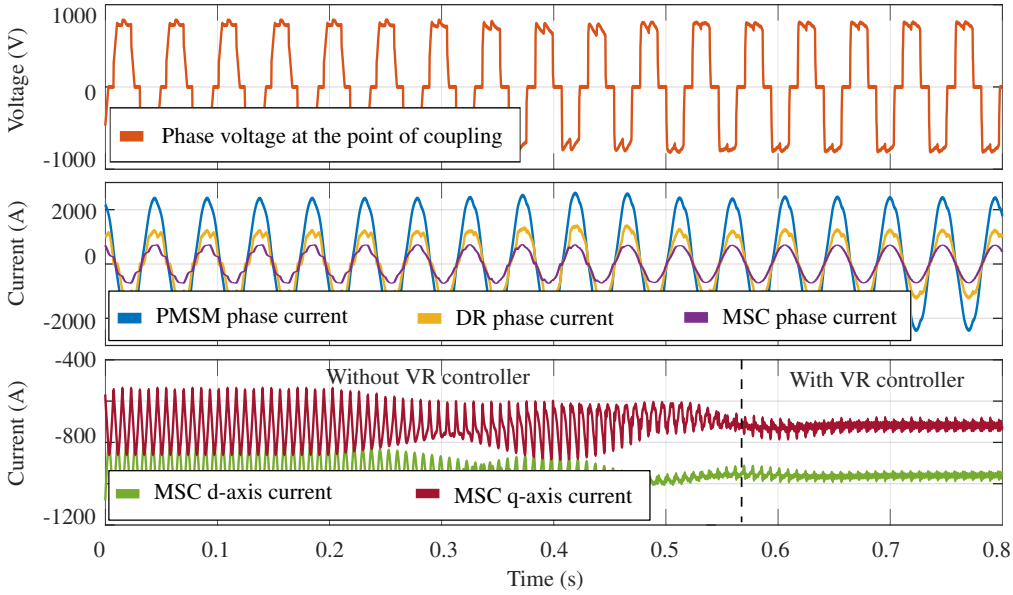

Fig. 3: Phase voltage and currents of the parallel drive PMSM, VSC and diode rectifier.

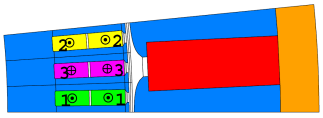

Fig. 4: Cross-section of one of the machine poles.

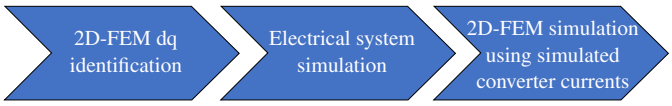

Fig. 5: Machine simulation process.

azimuth angle φ, and the tether length l [7, 4], whereas the orientation of the kite around the roll-axis is defined by a fourth state variable ψ.

Assuming a mass-less kite and the tether in a state of aerodynamic equilibrium with a homogeneous wind field along the x-axis, the dynamic and kinematic equations of motion can be simplified into a first-order system of equations

$$\dot{\psi} = g_k v_a \delta + \dot{\varphi} \cos\vartheta \tag{1}$$

$$\dot{\vartheta} = \frac{v_w}{l}(E\cos\vartheta\cos\psi - \sin\vartheta) - \frac{\dot{l}}{l}E\cos\psi \tag{2}$$

$$\dot{\varphi} = -\frac{v_w E\cos\vartheta - \dot{l}E}{l\sin\vartheta}\sin\psi \tag{3}$$

$$\dot{l} = v_{winch}, \tag{4}$$

where v_w is the wind speed, l is tether lengths, v_a is the apparent wind speed of the kite and E is the glide ratio.

The control system of the AWES comprises a central autopilot, which with the help of a flight controller defines the optimal flight trajectory of the kite. The steering dynamics are simplified in Equation (1) by the turn-rate law (TRL) $g_k v_a \delta$, where g_k is an empirical system parameter that quantifies the maneuvering response of the kite, and δ is a non-dimensional control input to the pod controller. A winch controller is used to calculate the optimal winching speed for maximum energy yield according to the method described in [4]. An overview of the kite system parameters is available in Table I.

PMSM Model

Two models for the PMSM are employed. The first is an analytical voltage behind reactance model used in the simulation environment of Fig. 2. The second is a 2D FEM model used for designing the machine and estimating its losses. The chosen electrical machine is a low-speed, high-torque 64-pole ferrite permanent magnet synchronous generator with an external rotor. The generator is rated for 690 V line-to-line RMS voltage and has a three-phase stator winding. The parameters of the electrical machine are listed in Table I, the cross-section of one pole of the machine 2D FEM model is depicted in Fig. 4.

Analysis and parametrization of the electrical machine can be understood with the help of Fig. 5. Starting with the FEM identification of the dq-model parameters with ideal current supply, the machine parameters can be identified. This data is then fed into the simulation model of Fig. 2 where the electrical current harmonics are calculated for each converter topology. These currents form the basis for the last step, where another FEM simulation is run to accurately determine the flux distribution, forces, and iron losses for each drive concept. The simulations are based on angular step-wise magneto-static FEM calculations with 192 angular steps per electrical period using FEMAG FEM software. Reference temperatures for all simulations are 120°C for the winding and 40°C for the magnets, respectively.

The losses are calculated and considered in a post-processing routine. For this purpose, the extended Jordan model with the loss density for each frequency component of the flux distribution is applied

Table I: System Parameters

Component	Parameter	Symbol	Value	Unit
Kite	Reel-out power	P_{mech}	1.8	MW
	Projected area	A	300	m^2
	Aerodynamic coef.	C_R	1	-
	Glide ratio	E	5	-
PMSM	Rated power	P_N	1.75	MW
	Rated volrage	U_N	690	V
	Rated torque	T_N	220	kNm
	Maximum speed	N_{max}	200	min^{-1}
	Rated power factor	$cos(\Phi_N)$	0.9	-
	Pair of poles	p	32	-
	d-axis inductance	L_d	0.74	mH
	q-axis inductane	L_q	0.95	mH
	Outer diameter	D_o	2240	mm
	Core length	L_{FE}	1200	mm
VSC/Boost converter	DC-link voltage	U_{DC}	1.2	kV
	Switching frequency	f_{sw}	2	kHz
	Decoupling inductor	L_f	800	μH
	Boost inductor	L_{boost}	277	μH
Reference IGBT/Diode Module	Reference module	-	[8]	-
	Reference heatsink	-	[9]	-
	LPF (IGBT)	f_{cr}	0.8, 8.7, 81.6, 304.2	Hz
	LPF (Diode)	f_{cr}	0.8, 8.4, 55.2, 130.1	Hz

according to

$$p_{fe} = \sum_v (c_{\mathrm{h}} \cdot f_v^{c_{\mathrm{f,h}}} + c_{\mathrm{w}} \cdot f_v^{c_{\mathrm{f,w}}}) \cdot B_v^{c_B}, \tag{5}$$

where c_{h} and $c_{\mathrm{f,h}}$ are the loss coefficients for hysteresis losses, c_{w} and $c_{\mathrm{f,w}}$ for eddy-current losses in the core material M600-50A. The eddy current losses in the magnets were calculated based on [10], but were found to be negligible because of the very low ferrite magnet electrical conductivity and hence are not considered further. Finally, the additional winding losses due to the current harmonics are calculated with the help of

$$p_{v,w} = m \cdot R_{1,DC} \cdot \sum_\mu k_{r,\mu}(f_\mu) \cdot I_\mu(f_\mu)^2, \tag{6}$$

where $k_{r,\mu}$ is the frequency dependent AC resistance rise factor caused by the current displacement due to the skin and proximity effects.

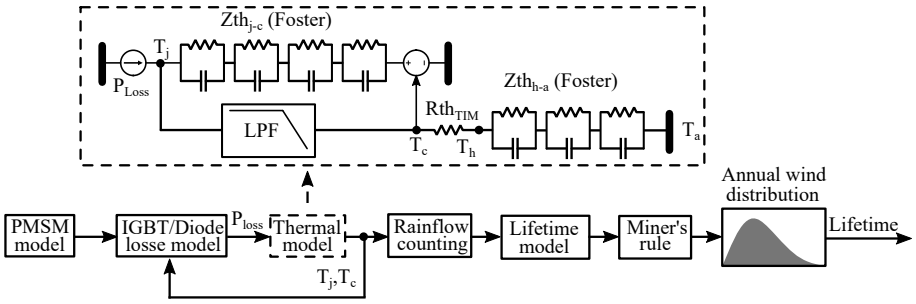

Fig. 6: Overview of the thermal and lifetime model.

Power Electronic Converter Thermal and Lifetime Models

Estimation of the converter lifetime is implemented according to Fig. 6. The converter losses are calculated from

$$P_{cond}(SF) = \left\{D, 1-D\right\} \cdot U_{on}\left(\frac{I}{SF}, T_j\right) \cdot I \tag{7}$$

$$P_{sw}(SF) = f_{sw} \cdot SF \cdot E_{sw}\left(U_{DC}, \frac{I}{SF}, T_j\right) \tag{8}$$

as a function of the discrete instantaneous duty cycle (D), device current (I), the junction temperature (T_j), and the silicon chip area scaling factor (SF) defined according to

$$SF = \frac{Chip\ Area^{\,new}}{Chip\ Area^{\,old}}. \tag{9}$$

The scaling assumes a linear relationship between the chip area and the power losses as explained in [11]. The thermal model of each discrete device (IGBT or diode) is modeled in the frequency domain according to the method described in [12], the calculated power module critical frequencies f_{cr} used in the low-pass filter (LPF) are listed in Table I. This method allows for better estimation of the power module case temperature when compared to the standard Foster model. The thermal resistance (R_{th}) is scaled according to

$$R_{th}^{scaled}(SF) = \frac{R_{th}^{base}}{SF}, \tag{10}$$

whereas the thermal time constant is assumed to remain constant regardless of the SF.

Finally, the number of thermal cycles for different wind speeds is calculated using the Rainflow counting algorithm. The empirical model in [13] is used to calculate the lifetime of the devices, while Miner's rule and a Weibull wind distribution at 300 m [14] are used to extend the calculation for one year. More details about the investigation algorithm can be found in [5].

In this work, the investigations in [5, 6] are further extended by examining the impact of wind turbulence on the lifetime of electrical system. Three different wind classes corresponding to offshore (c_0 case), open land (c_1 case), and agricultural land (c_2 case) [15] are considered.

Selection of Power Converter Topology

The parallel drive requires a DC-DC stage to serve the purpose of controlling the current of the passive diode rectifier, as well as to boost the unregulated rectifier voltage (U_{DR}) to the DC-Link voltage level ($U_{DC-Link}$), especially at lower operational speeds [16]. Two different DC-DC converter topologies are compared in this work. The first is the standard boost converter shown in Fig. 7a, which, when combined

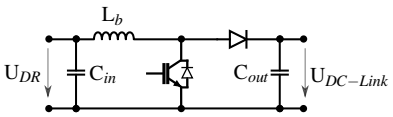

(a) Boost converter.

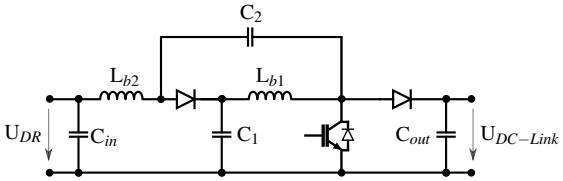

(b) Quasi Z-source converter.

Fig. 7: DC-DC converter topologies.

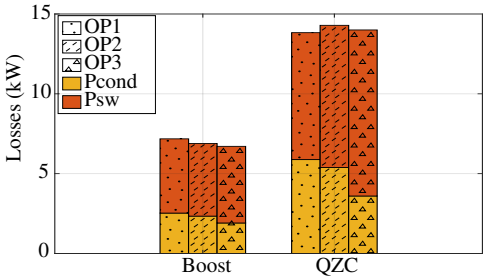

Fig. 8: DC-DC converter losses for different operating points. The machine speed in OP1, OP2 and OP3 is 0.1 pu, 0.5 pu, and 1 pu of the rated value respectively; the torque in all OPs is equal to the rated torque.

with the DR, provides a reliable and low cost topology that has been successfully commercialized in classical wind applications ranging from few kilowatts to several Megawatts [16].

The second considered topology is the quasi Z-source converter (QZC) shown in Fig. 7b. It is a member of the impedance network converter family which are characterized by their excellent voltage boost capability, reduced-size energy link, and higher reliability. The standard Z-source topology has been investigated for wind applications in [17]. The quasi variation is an improved version of the topology that exhibits lower stress on the components, a smaller sized energy link, and eliminated inrush current problem [18].

The topologies are compared in terms of the size and losses of the active components for three operating points. The dimesnioning results suggest that, in order to keep the device temperatures within the rated range, the QZC uses 50% more silicon chip area than the boost converter. A comparison of the losses is also depicted in Fig. 8. The results indicate that, regardless of the operating point, the boost converter produces roughly 50% fewer losses than the QZC while requiring 50% less silicon chip area. Therefore, the boost topology is considered a more viable option and has been used in later investigations.

Power Converter Lifetime Sizing and Efficiency

The dimensioning of the power electronic converters for both systems is conducted based on the target lifetime of 20 years, according to Fig. 6. The dimensioning is carried out for different control algorithms and wind classes. The impact of those variations can be understood with the help of Fig. 9 where speed, torque, and converter diode temperatures are plotted for a variable wind speed condition.

Two distinct kite controls are adopted, the first being a standard kite control (SKC) in which the machine reverses rotation under maximum torque. This causes large temperature spikes during this low-frequency operation as represented by the blue curve of Fig. 9d. The second kite control strategy was first introduced in [6]. This modified kite control strategy (MKC) allows for a slower transfer phase during which the torque drops by 20% to 60% of the rated value depending on the wind condition. The impact on the converter is also depicted by the yellow curve of Fig. 9d where the spikes in the diode junction temperature $T_{j,FWD}$ are clearly reduced. Another improvement to the control system considers the reduction of the switching frequency by 50% during this low-frequency operation. The impact on the VSC diode temperatures is depicted by the red and violet curves of Fig. 9d for the standard power converter system.

However, there remain temperature cycles because of the reel-out/reel-in duality of the system, which, according to [5] has the highest impact on the converter lifetime. The parallel drive concept tries to mitigate this problem by maintaining a relatively equal loading of the VSC during both phases, which reduces the temperature variation ΔT and prolongs the lifetime. This can be clearly seen by the blue curve of Fig. 9e. On the contrary, the rectifier and the boost converter would have to withstand much larger temperature variation ΔT as shown by the red and the yellow curves of Fig. 9e. The VSC power is

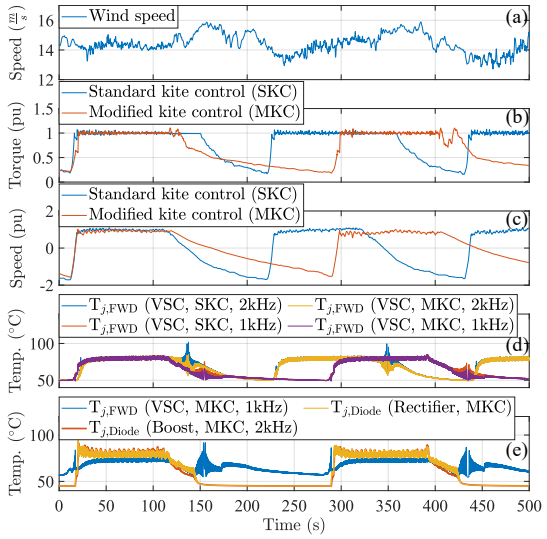

Fig. 9: FWD temperatures for the different control strategies and drive concepts.

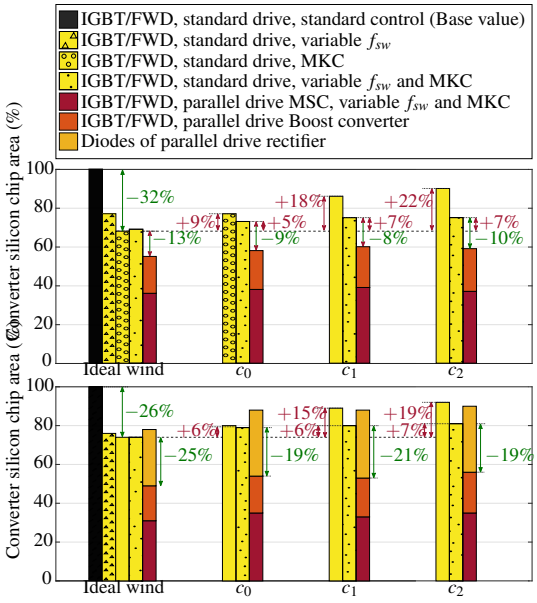

Fig. 10: Sizing results of the power converters for a target lifetime of 20 years.

also filtered with a frequency of 0.2 Hz. Therefore, temperature cycles due to wind turbulence are largely decoupled from the VSC as depicted in the same figure.

The impact of these different control strategies on the power converters sizing for a 20 years lifetime goal is shown in Fig. 10. The standard drive with standard control is taken as the base value (shown in black) to which all the other cases are compared. The results are depicted for four different wind conditions. They suggest that, under ideal wind conditions, the standard drive VSC size (shown in yellow) can be reduced by the largest margin when adopting a MKC strategy. This is not the case under turbulent wind conditions, where adopting a combined MKC and a lower switching frequency reduces the converter size the most. Also to be noticed is, depending on the wind class, the standard drive VSC would have to be over-scaled by up to 22% for the IGBT and 19% for the FWD compared to the ideal wind case. This is especially true for land installations in agricultural areas, whereas offshore installations require only an over-scalling of 9% and 6% for the IGBT and FWD respectively.

The impact of the parallel drive on the total converter size can be understood from the red variation bars of Fig. 10. Depending on the wind speed, the IGBT chip area can be further reduced by 8% to 13% compared to the standard drive with optimized control. The combined chip area of the VSC and the boost converter FWD's can be reduced by 19% to 25% respectively. There is, however, an additional diode chip area required for the DR. These silicon chips are usually much cheaper than the fast switching FWDs which should result in an overall cost reduction. This reduction is however compromised by the higher complexity of the system.

A breakdown of the converter losses for the rated operating point is depicted in Fig. 11. The results suggest that the VSC of the parallel drive generates fewer losses; the savings are compromised by the extra losses in the boost converter and the diode rectifier; The difference is however negligible. A better understanding can be deducted from Fig. 12 where the absolute difference in the efficiency of both drive concepts during the generation phase is shown. The difference is negligible for most operating points except for the very low-speed region around the speed reversal point.

Analysis of PMSM Performance and Efficiency

The PMSM performance variation between both drives is investigated for the generator operation only, as the motor operation mode is identical in both converters and thus not considered furthermore. While the current angle can be selected for the standard converter in such a way that optimal efficiencies are

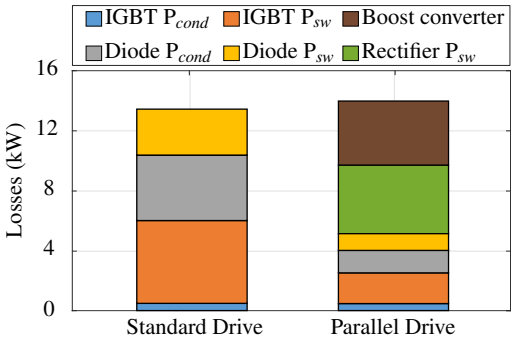

Fig. 11: Nominal losses of the converters.

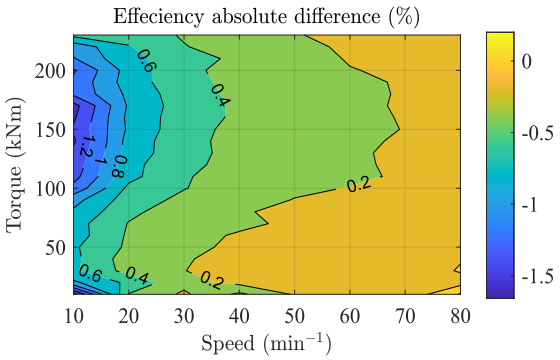

Fig. 12: Power converters efficiency difference. Positive values indicate the standard drive is better.

achieved in each operating point (efficiency optimization), this is not possible for the parallel converter because of the diode rectifier. The parallel converter current angles are therefore larger than in case of the standard converter as depicted in Fig. 13, which increases the field-weakening d-axis current and the resulting phase current for a given mechanical load. On the one hand, this results in higher winding losses as shown in Fig. 14. On the other hand, it reduces the main magnetic flux, which reduces the iron losses. Furthermore, additional winding and iron losses are caused by the current harmonics created by the DR.

An indicator of the current harmonics loss contribution is the total harmonic distortion (THD) depicted in Fig. 15, which describes the relation of the amplitudes of the harmonics to the fundamental amplitude. It should be noted that these harmonics flow only through the DR and not the VSC. This is accomplished by using several vector-resonant controllers [6] as shown in Fig. 2. However, the THD remains below 20% for all generator operating points. The additional winding losses due to the current harmonics are roughly proportional to the square of the THD if the AC resistance rise factor $k_{r(f)}$ caused by the current displacement is neglected. Otherwise, the current displacement increases the winding resistance with growing frequencies.

Because of the large reluctance in the magnetic circuit (main flux saturation and large paths with low permeability through the air gap and magnets), a significant amount of current is needed to build a magnetic flux capable of increasing the machine iron losses. Since the THD of the current is on average around 10% and field weakening current is higher for the parallel converter, the current harmonics almost only lead to an increase in winding losses, while iron losses remain comparable for both drives. Fig. 16 demonstrates that the current harmonics also lead to a considerable increase in the torque oscillations.

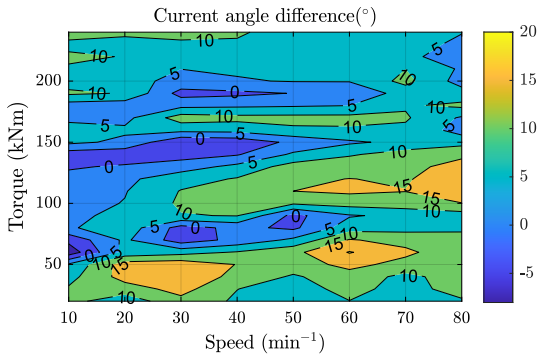

Fig. 13: PMSM current angle difference between standard and parallel drives. Positive values indicate the standard drive is better.

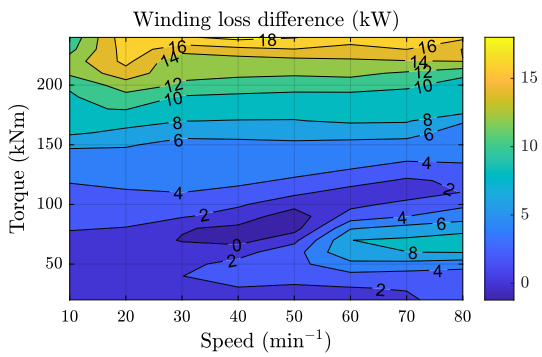

Fig. 14: Winding loss difference between the standard and parallel drives. Positive values indicate the standard drive is better.

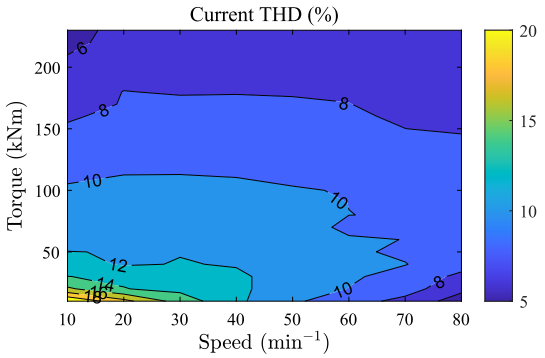

Fig. 15: Machine current THD for the parallel drive.

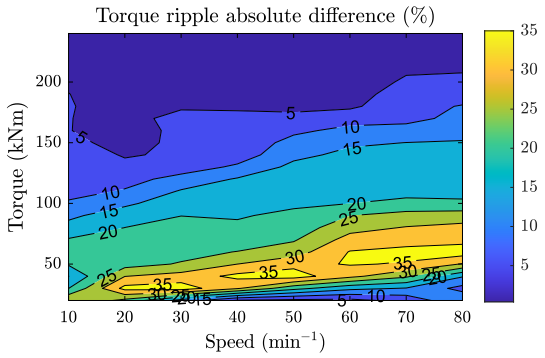

Fig. 16: Torque ripple difference. Positive values indicate the standard drive is better.

The magnetic noise emission of the machine is therefore likely to increase.

The PMSM efficiency for the standard drive stands out to be highly efficient at higher generative speeds and less efficient for low-speed high-torque operation points, as needed in the transfer phase. This effect is even worse when the machine is fed by the DR. In Fig. 17, the efficiency of the parallel converter fed generator is compared with the efficiency of the standard converter fed generator. On average, the efficiency of the parallel converter fed generator is only around 1% lower. At low speeds with high loads, the decrease in efficiency is higher. However, the modified kite control strategy reduces the impact of the low transfer phase efficiency by flying the kite at lower torques, thus avoiding the low-efficiency region of the machine.

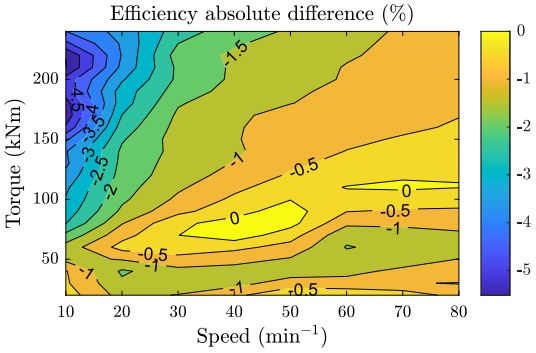

Fig. 17: Generator efficiency. Negative values indicate the standard drive is better.

Conclusion

In this work, two power drive systems and two control strategies were analyzed and compared in terms of their impact on the power electronic converter size, the machine performance, and the overall system efficiency. We concluded that adjusting the transfer phase kite control to allow for a lower torque during speed reversal could reduce the required converter size by around one-third.

Using a novel parallel power converter concept comprising a voltage source converter paralleled with a diode rectifier was investigated for decoupling the effect of reel-out/reel-in thermal cycles. It was found that the IGBT chip area can be reduced by an additional 13% compared to the standard drive concept with adjusted control, while the required fast switching diode chip area is expected to decrease by roughly 25%. However, an additional 30% of slow cheap diodes are required for the passive diode rectifier. The total cost should however remain lower since the significant saving of the expensive IGBTs and FWD's should outweight the slight increase in the cheap rectifier cost. The impact of the parallel drive on the power converter efficiency was found to be negligible.

The impact of the installation location for different wind classes was also looked at. It was concluded that onshore installations could increase the required converter size anywhere between 5% to 22% depending on the control strategy and the roughness of the surrounding terrains. On the contrary, offshore installations would require only a marginal over-sizing of the power converters.

The impact of the parallel converter concept on the PMSM was also analyzed. The results indicate that the machine efficiency decreases by less than 1% around the rated operating range. This value increases to 5% at very-slow high-torque regions required during the transfer phase. This operating range can however be avoided by opting for the modified kite control strategy. The impact of the diode rectifier current harmonics on the machine was also investigated. It was concluded that the PMSM current has a THD of 10% on average, which gives rise to torque ripples and could increase the machine acoustic noise emissions.

References

[1] S. P. GmbH, "SkySails Power GmbH Image Brochure." https://skysails-group.com/downloads/.

[2] M. Diehl, U. Ahren, and R. Schmehl, *Airborne Wind Energy*. Springer, Berlin, Heidelberg, 2013.

[3] S. P. GmbH, "Kite Power For Mauritius." https://skysails-power.com/kite-power-for-mauritius/.

[4] M. Erhard and H. Strauch, "Flight control of tethered kites in autonomous pumping cycles for airborne wind energy," *Control Engineering Practice*, vol. 40, pp. 13–26, July 2015.

[5] B. Bagaber, P. Junge, and A. Mertens, "Lifetime Estimation and Dimensioning of the Machine-Side Converter for Pumping-Cycle Airborne Wind Energy System," in *2020 22nd European Conference on Power Electronics and Applications (EPE'20 ECCE Europe)*, Sept. 2020.

[6] B. Bagaber and A. Mertens, "A Parallel Voltage Source Converter and Diode Rectifier PMSM Drive Concept for Decoupling the Thermal Cycles in the Machine-Side Converter of an Airborne Wind Energy Generator," in *2021 23rd European Conference on Power Electronics and Applications (EPE'21 ECCE Europe)*, Sept. 2021.

[7] M. Erhard and H. Strauch, "Control of Towing Kites for Seagoing Vessels," *IEEE Transactions on Control Systems Technology*, vol. 21, pp. 1629–1640, Sept. 2013.

[8] ABB, "Data Sheet, Doc. No. 5SYA 1461-01 10-2020: 5SNA 2400N170300 HiPak IGBT Module."

[9] SEMIKRON, "SEMIKRON_DataSheet_SKiiP_2414_GB17E4_4DUW_V2_20603236."

[10] D. Zhang, A. Ebrahimi, C. Wohlers, J. Redlich, and B. Ponick, "On the analytical calculation of eddy-current losses in permanent magnets of electrical machines," in *IECON 2020 The 46th Annual Conference of the IEEE Industrial Electronics Society*, pp. 1052–1056, Oct. 2020.

[11] A. Merkert, T. Krone, and A. Mertens, "Characterization and Scalable Modeling of Power Semiconductors for Optimized Design of Traction Inverters with Si- and SiC-Devices," *IEEE Transactions on Power Electronics*, vol. 29, no. 5, pp. 2238–2245, 2014.

[12] K. Ma, M. Xu, and B. Liu, "Modeling and Characterization of Frequency-Domain Thermal Impedance for IGBT Module Through Heat Flow Information," *IEEE Transactions on Power Electronics*, vol. 36, pp. 1330–1340, Feb. 2021.

[13] ABB, "Application Note 5SYA 2043-04 : Load-cycling capability of HiPak modules."

[14] K. D. Centre, "Dutch Offshore Wind Atlas." https://data.knmi.nl.

[15] T. Haas and J. Meyers, "AWESCO Wind Field Datasets [Data set]," *Zenodo*, 2019.

[16] V. Yaramasu, B. Wu, P. C. Sen, S. Kouro, and M. Narimani, "High-power wind energy conversion systems: State-of-the-art and emerging technologies," *Proceedings of the IEEE*, vol. 103, pp. 740–788, May 2015.

[17] U. Supatti and F. Z. Peng, "Z-source inverter based wind power generation system," in *2008 IEEE International Conference on Sustainable Energy Technologies*, pp. 634–638, Nov. 2008.

[18] O. Ellabban and H. Abu-Rub, "Z-Source Inverter: Topology Improvements Review," *IEEE Industrial Electronics Magazine*, vol. 10, pp. 6–24, Mar. 2016.